mathematics

MDPI

Article

Transformerless Partial Power AC-Link Step-Down Converter

Rodrigo A. Bugueño [1,†], Hugues Renaudineau [1,2,†], Ana M. Llor [1,3,†] and Christian A. Rojas [1,2,*]

[1] Department of Electronics, Universidad Técnica Federico Santa María, Valparaíso 2390123, Chile; rodrigo.bugueno@sansano.usm.cl (R.A.B.); hugues.renaudineau@usm.cl (H.R.); ana.llor@usm.cl (A.M.L.)
[2] Advanced Center for Electrical and Electronic Engineering, Valparaíso 2390123, Chile
[3] Electronics Engineering Department, Université de Toulouse, LAPLACE, 31062 Toulouse, France
* Correspondence: christian.rojas@usm.cl
† These authors contributed equally to this work.

Abstract: DC–DC power converters are essential for various applications, including photovoltaic systems, green hydrogen production, battery charging, and DC microgrids. Partial Power Converters (PPC) are notable for their efficiency, processing only a fraction of total power and reducing conversion losses, but this performance is overshadowed by the high cost of its construction, associated with high-frequency transformers (HFT). This paper introduces a transformerless partial power AC-link step-down converter, eliminating the need for an HFT and reducing costs while improving power density. An experimental validation using a reduced-scale prototype demonstrates the converter's operation with a peak efficiency of 93.2% and overall efficiency above 92%, demonstrating the experimental viability of the converter. The proposed AC-link seen as a two-port network is shown to be very attractive for DC–DC step-down operations, and as a possible replacement of traditional PPC.

Keywords: DC–DC converter; non-isolated full-bridge converter; partial power converter; transformerless AC-link

MSC: 94C05

check for updates

Citation: Bugueño, R.A.; Renaudineau, H.; Llor, A.M.; Rojas, C.A. Transformerless Partial Power AC-Link Step-Down Converter. *Mathematics* **2024**, *12*, 1939. https://doi.org/10.3390/math12131939

Academic Editor: Kotb Basem Tawfiq

Received: 21 May 2024
Revised: 14 June 2024
Accepted: 20 June 2024
Published: 22 June 2024

Copyright: © 2024 by the authors. Licensee MDPI, Basel, Switzerland. This article is an open access article distributed under the terms and conditions of the Creative Commons Attribution (CC BY) license (https://creativecommons.org/licenses/by/4.0/).

1. Introduction

Today, the world is immersed in energy transition, seeking new ways to phase out fossil fuels [1]. DC–DC converters play a vital role in controlling and regulating electric energy [2]. In electricity generation, DC–DC converters are essential for photovoltaic applications, where they are responsible for controlling the input power of the systems [3]. Furthermore, in the transportation sector, DC–DC converters are required to regulate the output power for battery charging, particularly in electric cars and other vehicles powered by different energy sources. On the other hand, DC–DC converters in microelectronics and the next generation of data centers are fundamental for Voltage Regulation Modules and Power Management Integrated Circuits [4].

For all the aforementioned applications, power electronics converters play a vital role, since they allow controlling and regulating the electric energy [5]. Because of the DC nature of the various elements constituting those systems (e.g., PV, battery, water electrolyzers, fuel cells), DC–DC converters have become of main interest, and are fundamental in the context of DC microgrids and smart transformers [6]. Traditional buck and boost converters are still widely used in the academic literature [7], as for example, buck converters for electrolysis [8], or boost converters for li-ion batteries [9] and fuel cell systems [10]. However, there is a trend toward more advanced topologies, with a huge number of DC–DC converter alternatives [5,11].

Among all, the concept of PPC is a very attractive solution that has attracted a lot of attention in recent years [2,12]. Traditional full-power converters, illustrated through Figure 1a, process the entire input-to-output power of the DC–DC conversion stage. On

the other hand, PPC (Figure 1b,c) has the unique characteristic of processing only a fraction of the total power, leading to improved efficiency compared to classical full-power topologies [12]. It also has higher power density and results in cost reduction thanks to the lower rating of the components, without sacrificing functionality [2]. As can be seen in Figure 1, PPC only processes a fraction of the total power, while the rest is directly fed to the load through a direct path.

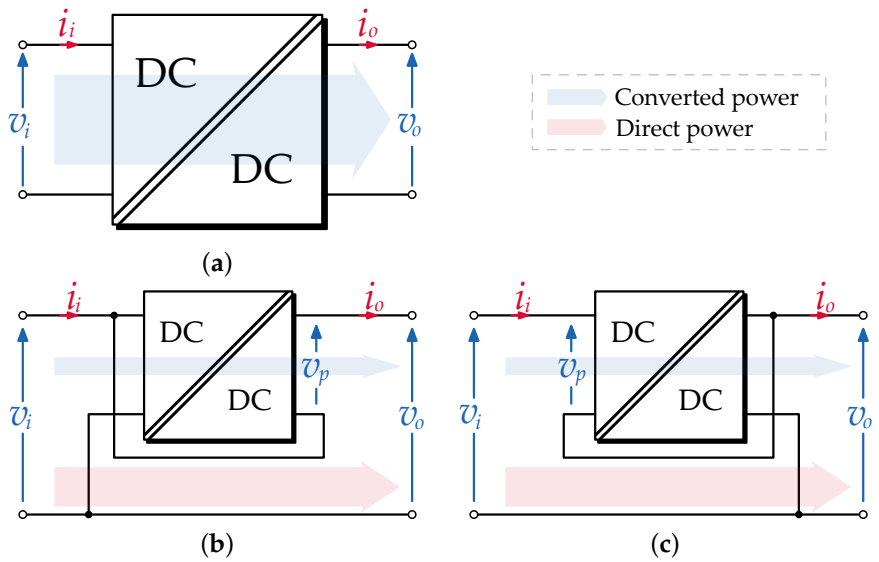


Figure 1. PPC concept illustration—(**a**) traditional full-power converter, (**b**) IPOS step-up PPC (Type I), (**c**) ISOP step-down PPC (Type II).

PPC can be divided into two categories, depending on the converter interconnection. First, input-parallel output-series (IPOS), also known as type I PPC [2,12,13], as represented in Figure 1b in its step-up version. Input-series output-parallel (ISOP) PPC can also be used (also known as type II PPC [2,12,13]) and is represented in Figure 1c in its step-down configuration. For all their advantages, PPCs have been applied in a large number of applications including PV systems [14,15], batteries [16], electrolysis [17], and EV charging stations [18].

However, the main drawback of PPCs is their dependence on HFT, which contributes to the cost, weight, and size of these converters. This issue is further compounded by the fact that, due to the specific interconnection typical of PPCs, they result in a solution without galvanic isolation despite utilizing a transformer. To deal with this issue, this paper proposes a transformerless partial power AC-link converter for step-down DC–DC applications as shown in Figure 2a and its experimental implementation and validation. The proposed converter considers an impedance network, hereafter referred to as AC-link, instead of HFT as used in conventional PPCs (Figure 2b). The conceptual idea of this new converter family has been introduced in [19]. Preliminary results obtained through simulation can be found in [20] applied for step-down (Buck) for photovoltaic integration to a DC microgrid. A step-up (Boost) version of this converter can be found in [21] applied for an electric-vehicle fast charging station. In this paper, experimental results of the transformerless partial power AC-link step-down DC–DC converter in an open-loop operation are provided to validate the proposed converter. Closed-loop operation is outside the scope of this paper, thus the application can be considered a general DC–DC conversion due to the versatility of this converter. The technical motivations of this work are: (i) to avoid the use of HFT in partial power DC–DC converters to reduce costs, (ii) to develop a reduced order model for this converter, and (iii) to experimentally validate the proposed AC-link step-down DC–DC converter.

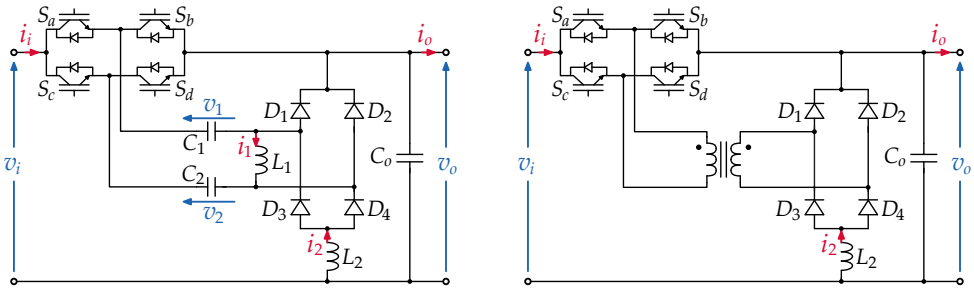


Figure 2. Proposed transformerless partial power step-down converter topology: (**a**) Proposed transformerless partial power step-down converter topology. (**b**) Traditional full bridge partial power step-down converter topology.

Main contributions of this paper are summarized as follows. Firstly, a prototype of the proposed transformerless partial power AC-link step-down converter is constructed and subjected to comprehensive experimental testing, validating its dynamic and steady-state performance in DC–DC conversion. Secondly, the paper offers a detailed and experimentally validated model of the converter, essential for controlling it effectively in specific applications, under both steady-state and dynamic conditions. Thirdly, the traditional PPC counterpart is experimentally implemented, enabling a direct comparison with the proposed converter, thereby showcasing the enhancements introduced by the solution proposed in this paper. Lastly, the paper includes a comparative analysis with selected converters possessing similar characteristics, affirming the relevance of the proposed transformerless partial power AC-link step-down converter and its potential applicability across various renewable energy applications. In summary, the specific advantages of eliminating the HFT by the proposed AC-Link converter in terms of peak efficiency, cost, cost per Watt, and power density, compared to a conventional PPC rated a 300 W are listed as follows:

- Peak efficiency is improved from 92% to 93.2% by using a gain voltage of $G_v = 0.5$.
- Cost is reduced from \$346 to \$184.
- Cost per Watt is reduced from 1.15 \$/W to 0.62 \$/W.
- Power density is increased from 2.0 3W/cm^3 to 2.78 W/cm^3.

Regarding the organization of the content, it is as follows. First, in Section 2, the converter operation is described, and a reduced-order dynamic average model is theoretically derived. Then, Section 3 presents experimental validation of the proposed converter on a reduced-scale laboratory prototype, including steady-state and dynamic results, voltage gain, and efficiency analysis and comparison with theory. Section 4 provides experimental comparison of the proposed converter with traditional PPC, and a comparison with other state-of-the-art DC–DC converters. Finally, Section 5 summarizes main ideas and results obtained.

2. Proposed Converter

2.1. Converter Topology

The proposed topology, which is shown in Figure 2a, consists of a controlled full bridge (S_a–S_d) connected through an AC-link to a diode H-bridge (D_1–D_4), which is grounded via an inductor (L_2). The AC-link comprises two capacitors (C_1, C_2) and an inductor (L_1). Finally, the converter has an output capacitor (C_o). Switching signals $\{s_a, s_b, s_c, s_d\}$ are defined, where $s_{a,c} = \{0, 1\}$, $s_b = 1 - s_a$ and $s_d = 1 - s_c$. Similar to classical PPC [12], a Phase-Shift Modulation (PSM) is employed. The PSM is characterized by a switching frequency f_{sw} and a displacement factor α between s_a and s_c, ranging from 0 to 0.5 per unit relative to a shifting angle between 0° and 180°, respectively. Note that the proposed converter is designed for unidirectional DC–DC applications. Bidirectional operation can be obtained by replacing the diode bridge with controlled semiconductors. This change is out of the scope of this paper.

A traditional PPC counterpart (Figure 2b) which has a full bridge (FB)-based step-down ISOP PPC (Type II), with HFT is also considered, since it will be experimentally implemented for comparison with the proposed solution. For both topologies, partial power ratio K_{pr}, defined as the ratio between converter power and total power of the conversion stage, follows [13]:

$$K_{pr} = 1 - G_v, \tag{1}$$

where $G_v = v_o/v_i$ is the input-to-output voltage gain of the conversion stage. This partial power ratio shows the importance of PPC. The lower it is, the lower the converted power, leading to improvements in terms of efficiency, component rating, power density, etc. . ., as has been described previously. For example, for an output voltage of half the input voltage $v_o = v_i/2$, the converter of the PPC will only face half the conversion stage power since $K_{pr} = 50\%$. In terms of reliability and lifespan, the proposed AC-link converter presents the drawback of adding additional capacitors, but it also have the advantage of lower stress on the semiconductors compared to classical PPC, leading to similar reliability.

2.2. Converter Operation

Depending on the value of α, the converter presents four possible operation states [20], as detailed in Table 1. In state S1, only diodes D_1 and D_4 are active, enabling the charging of the inductors via the voltage difference across capacitor C_1 and discharging part of the current through capacitor C_2. In state S2, all diodes are active, keeping inductor L_1 floating due to the short circuit created by the conduction of these diodes. Consequently, given the equivalent circuit obtained, the current from L_2 begins to flow in the reverse direction, slightly discharging this component. In state S3, only diodes D_2 and D_3 are active, resulting in a situation similar to state S1, except that capacitors C_1 and C_2 are in opposite positions, causing the current from inductor L_1 to flow in the opposite direction. Finally, in state S4, only diodes D_3 and D_4 are active; this causes inductor L_1 to remain floating again, and additionally, the input source becomes floating, allowing the output capacitor to slightly discharge through the remaining components of the circuit.

Table 1. Converter states: State S1: S_a and S_d are active; State S2: S_a and S_c are active; State S3: S_b and S_c are active; State S4: S_b and S_d are active.

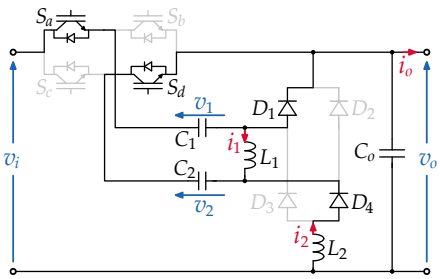
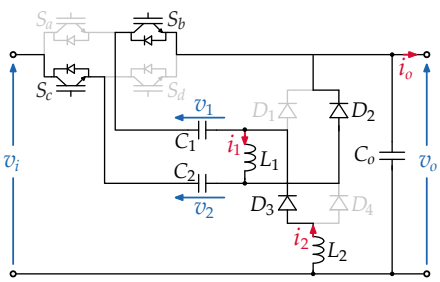
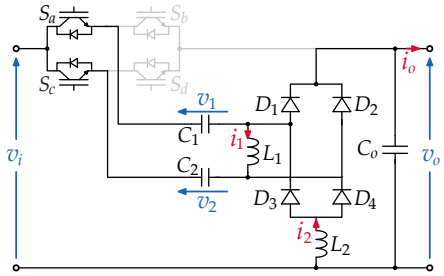
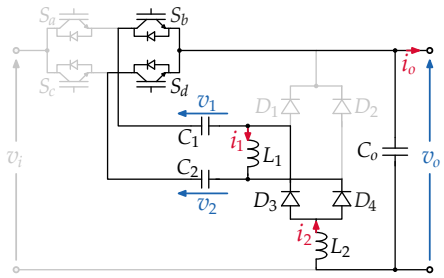
	Converter Operation	**State Variable Equations**
State S1: $t \in [0,\ \alpha T]$		$L_1\frac{di_1}{dt} = v_2$ $L_2\frac{di_2}{dt} = v_2 - v_o$ $v_1 = v_i - v_o$ $C_2\frac{dv_2}{dt} = -i_1 - i_2$ $-C_1\frac{dv_1}{dt} + C_o\frac{dv_o}{dt} = i_2 - i_o$
State S3: $t \in [T/2,\ (1/2-\alpha)T]$		$L_1\frac{di_1}{dt} = -v_1$ $L_2\frac{di_2}{dt} = v_1 - v_o$ $C_1\frac{dv_1}{dt} = i_1 - i_2$ $v_2 = v_i - v_o$ $-C_2\frac{dv_2}{dt} + C_o\frac{dv_o}{dt} = i_2 - i_o$

Table 1. *Cont.*

	Converter Operation	State Variable Equations
State S2: $t \in [\alpha T\ ,\ T/2]$		$L_1 \frac{di_1}{dt} = 0$ $L_2 \frac{di_2}{dt} = v_1 - v_i$ $v_1 = v_i - v_o$ $v_2 = v_1$ $-C_1 \frac{dv_1}{dt} - C_2 \frac{dv_2}{dt} + C_o \frac{dv_o}{dt} = i_2 - i_o$
State S4: $t \in [(1/2 - \alpha)T\ ,\ T]$		$L_1 \frac{di_1}{dt} = 0$ $L_2 \frac{di_2}{dt} = v_2 - v_o$ $v_1 = v_2$ $C_2 \frac{dv_2}{dt} + C_1 \frac{dv_1}{dt} = -i_2$ $C_o \frac{dv_o}{dt} = i_2 - i_o$

It is worth noting that the state variable equations exhibit some discontinuities that makes the full switched model unobtainable without including some equivalent series resistance (ESR) or another parasitic elements. These discontinuities were presented specifically in the voltage equations across the capacitors, forcing voltage steps between these sources and causing high current peaks as result. These suppositions are confirmed through converter simulations using the PLECS software, which requires minimal values for these parasitic elements.

Despite that, it is possible to obtain the state space waveforms that are depicted in Figure 3, for $\alpha = 0.4$ and $\alpha = 0.2$. In this simulation, the converter works with the parameters presented in Table 2, with a resistive output load of $R_o = 10\ \Omega$. It is observed in Figure 3(ii), that the current of inductor L_1 remains constant in states S2 and S4 in both scenarios, as previously described with a mean value close to zero and an amplitude of 3.78 A and 2.12 A, respectively. The alternating behavior exhibited by this current resulted in its AC-link denomination. On the other hand, in Figure 3(iii), it is noted that the current of inductor L_2 has an average value of $\bar{i_2} = 2.45$ A and $\bar{i_2} = 2.36$ A with a ripple of 9.7% and 26.2%. In Figure 3(iv), it is observed that both voltages of the link capacitors maintain a similar average value of $\bar{v_1} \approx \bar{v_2} \approx 52.8$ V and $\bar{v_1} \approx \bar{v_2} \approx 59.1$ V and exhibit a ripple lower than 1% for each α value respectively. Finally, the output voltage displays a considerably smaller ripple compared to the previous case staying inferior to 0.1%, but with a lower average voltage of $v_o = 47.0$ V and $v_o = 40.8$ V according to α.

Table 2. Simulation and experimental system parameters.

Parameter	Value	Unit
Input Voltage v_i	100	V
Switching Frequency f_{sw}	10	kHz
Dead Time dt	1	µs
AC-link Inductor L_1	0.56	mH
Output Inductor L_2	2.00	mH
AC-link Capacitors C_1 & C_2	1000	µF
Output Capacitor C_o	2200	µF

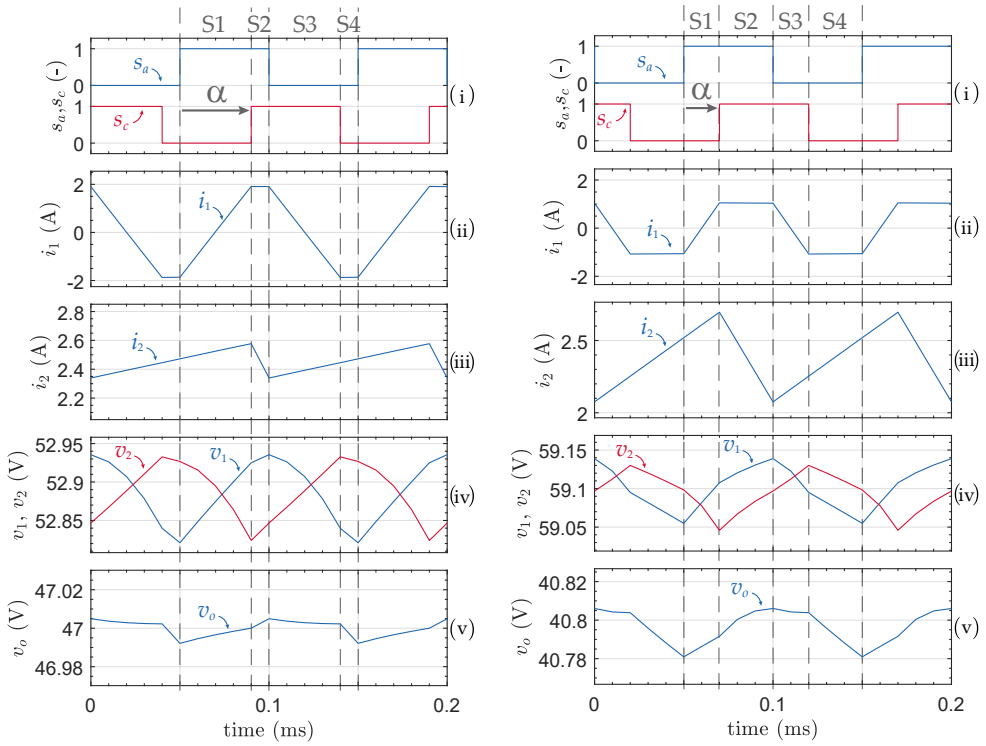


Figure 3. Simulation waveforms of the state variables of the converter: (**a**) $\alpha = 0.4$; (**b**) $\alpha = 0.2$. (i) Switching signals s_a and s_c; (ii) AC-link inductor current i_1; (iii) Output inductor current i_2; (iv) AC-link capacitors voltages v_1 and v_2; (v) Output capacitor voltage v_o.

2.3. Converter Mathematical Modeling

Due to the high-order, nonlinearity, and discontinuity described previously, mathematical modeling of the converter is not trivial. Thus, a reduced-order dynamic average model is adopted to represent the behavior of the proposed converter, while simplifying the equations. The average model is based on the average value of a signal defined by (2), where $T = 1/f_{sw}$.

$$\bar{x}(t) = \frac{1}{T}\int_{t}^{t+T} x(\tau)d\tau. \tag{2}$$

Furthermore, the AC-link dynamics of v_1, v_2 and i_1 are assumed to be negligible, as they are significantly faster compared to the dynamics associated with capacitor C_o and inductor L_2, due to its switched nature. The simplified hypothesis corresponds to:

$$\bar{v_1} - \bar{v_2} = 0 \tag{3}$$

$$\bar{v_1} + \bar{v_o} = \bar{v_2} + \bar{v_o} = \bar{v_i}. \tag{4}$$

In this case, states equations presented in Table 1 can be summarized to the average model presented in:

$$L_2\frac{d\bar{i_2}}{dt} = (0.5 + \alpha)v_i - (1.5 + \alpha)\bar{v_o} \tag{5}$$

$$(C_o + C_1 + C_2)\frac{d\bar{v_o}}{dt} = (1.5 + \alpha)\bar{i_2} - \bar{i_o}. \tag{6}$$

Considering the system in (5)–(6), the input-to-output voltage transfer function $H_v(s)$ of the system is obtained, as follows:

$$H_v(s) = \frac{\bar{v}_o(s)}{\bar{v}_{in}(s)} = \frac{\alpha^2 + 2\alpha + 0.75}{(C_o + C_1 + C_2)L_2 s^2 + (\alpha + 1.5)^2}. \tag{7}$$

Finally, assuming steady-state conditions, i.e., $s = 0$, the voltage gain G_v of the converter is given by:

$$G_v(\alpha) = \frac{\bar{v}_o}{\bar{v}_i} = \frac{1 + 2\alpha}{3 + 2\alpha}. \tag{8}$$

From (8), it is clear that the converter is capable of bucking the voltage between a factor of 0.33 and 0.5, depending on the phase shift α. Note that if $\alpha = [0,\ 0.5]$, then $G_v = [0.33,\ 0.50]$, i.e., the input voltage v_i and output voltage v_o cannot be close. Other advanced DC–DC topologies, such as partial power processing converters [12], are preferred in the case where v_i is similar to v_o to achieve reduced power at high efficiency. Alternative AC-link configurations can be used to extend the voltage reduction range.

2.4. Passive Components Sizing

Considering the mathematical model in (5)–(6), the input-to-output current transfer function $H_i(s)$ of the system is obtained as follows:

$$H_i(s) = \frac{\bar{i}_2(s)}{\bar{i}_o(s)} = \frac{1.5 + \alpha}{(C_o + C_1 + C_2)L_2 s^2 + (\alpha + 1.5)^2}. \tag{9}$$

and assuming steady-state conditions, the current gain G_i of the converter is also defined as

$$G_i(\alpha) = \frac{\bar{i}_2}{\bar{i}_0} = \frac{2}{3 + 2\alpha} \tag{10}$$

It is then possible to determine the required size of each passive components of the converter considering the following set of equations:

$$\begin{cases} L_1 = V_i \dfrac{(1 - G_v(1/2))}{2 f_{sw} \Delta i_1} \\ L_2 = V_i \dfrac{G_v(0)}{2 f_{sw} \Delta i_2} \\ C_p = V_i \dfrac{G_v(0) G_i(0)}{2 f_{sw} R_o \Delta v_p} \\ C_o = V_i \dfrac{G_v(0)(G_i(0) - 1)}{2 f_{sw} R_o \Delta v_o} \end{cases} \tag{11}$$

where $C_p = C_1 + C_2$, $v_p = v_1 = v_2$, and $C_1 = C_2$. Considering a resistive load $R_o = 10\,\Omega$, and parameters of Table 2, maximum ripple of variables i_2, v_p y v_o are $\Delta i_2 = 37.5\%$, $\Delta v_1 = \Delta v_2 = 0.038\%$, and $\Delta v_o = 0.167\%$. For the current i_1, being an AC waveform, it maximum amplitude is set as $I_1 = \Delta i_1 / 2 = 2.232$ A.

3. Experimental Validation

To validate the proposed converter, an experimental down-scale prototype, shown in Figure 4, was constructed using SKM100GB12T4 IGBT semiconductors; a PCV-2-564-08L inductor as L_1, LGL2G102 capacitors as C_1 and C_2, and a B43564A0228 capacitor as C_o, using parameters previously presented in Table 2. Given that this is a proof of concept, the system is built with a wide power limit of up to 1 kW. The prototype uses a dSpace MicrolabBox 1202/1302 as a DSP/FPGA unit to implement the PSM algorithm and generate the four switching signals required for converter operation. The switching signals are transmitted via optical fiber (FO) using an FO board to the gate driver boards to mitigate potential noise issues. The gate drivers condition the signals for switching using a gate resistor $R_g = 3\,\Omega$. Depending on the test, either a regenerative power supply or a resistive load $R_o = 10\,\Omega$ will be used.

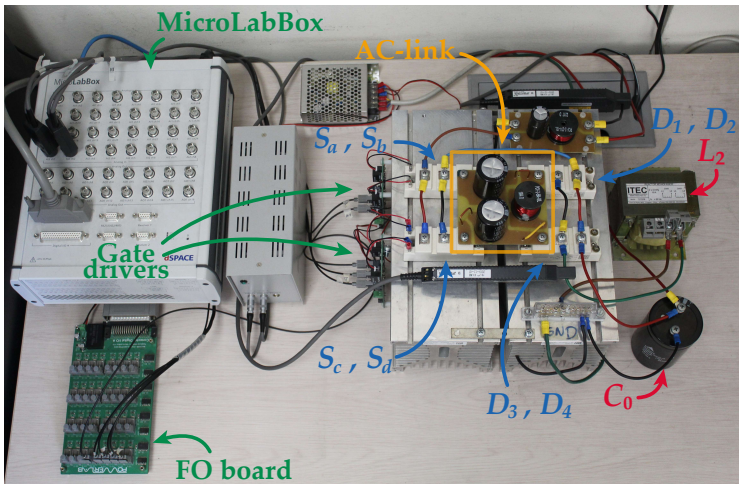


Figure 4. Experimental prototype of the partial power AC-link converter.

3.1. Steady-State Results

In this test, $\alpha = 0.4$ and $\alpha = 0.2$ are selected to showcase the characteristic variations between states and enable a comparison with the waveforms obtained previously in Figure 3. Figure 5 displays the steady-state waveforms of state variables obtained in the converter, using a time scale of 50 µs/div to present five periods of the waveforms.

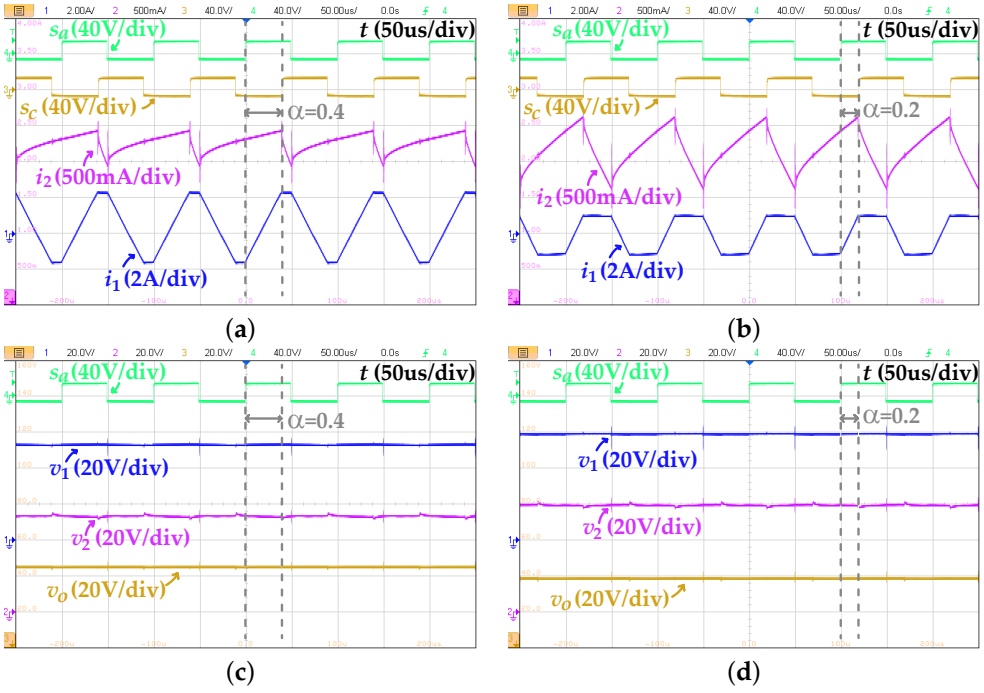


Figure 5. Experimental results of the system for different values of α: (**a**) s_a and s_c gate-source voltages, AC-link inductor current i_1 and output inductor current i_2 with $\alpha = 0.4$; (**b**) s_a and s_c gate-source voltages, AC-link inductor current i_1 and output inductor current i_2 with $\alpha = 0.2$; (**c**) s_a gate-source voltage, AC-link capacitor voltages v_1 and v_2, and output capacitor voltage v_o with $\alpha = 0.4$; (**d**) s_a gate-source voltage, AC-link capacitor voltages v_1 and v_2, and output capacitor voltage v_o with $\alpha = 0.2$.

Figures 5a,b illustrate both inductor currents, where waveforms depend on the phase shift between s_a and s_c. The AC-link inductor current i_1 exhibits the well-known charge and discharge behavior of the presented states, while the output inductor current i_2 exhibits different slopes associated with the corresponding states presented in Table 1.

Figures 5c,d show the voltage across all capacitors in the circuit. These signals exhibit almost continuous values, with small ripple depending on the converter's commutation state, which is barely noticeable as the ripple magnitude is lower than 1%. The obtained mean voltage values for $\alpha = 0.4$ are $\bar{v_1} = 52.96$ V, $\bar{v_2} = 53.17$ V and $\bar{v_o} = 46.00$ V, whereas, the obtained values for $\alpha = 0.2$ are $\bar{v_1} = 59.11$ V, $\bar{v_2} = 59.11$ V and $\bar{v_o} = 39.66$ V. These results allow us to validate the simplifying hypothesis of (3) and (4).

Figure 6 presents a comprehensive comparison between simulation and the experimental results. The similarity between the two results is apparent for both values of α, but the most notable difference lies in the output inductor current i_2, where the observed waveform sightly deviates from the expected ideal triangular waveform and a minimal static error in the output capacitor voltage v_o due to the presence of losses in the prototype. Specifically, errors of 5.29% and 6.48% between simulated and experimental output voltage v_o were presented, for $\alpha = 0.4$ and $\alpha = 0.2$, respectively.

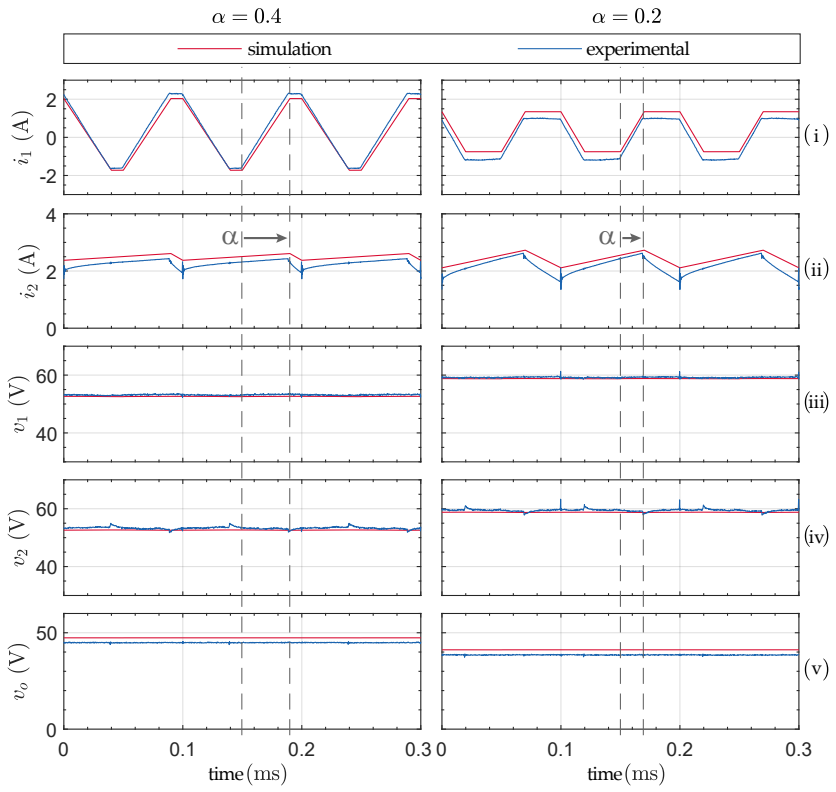
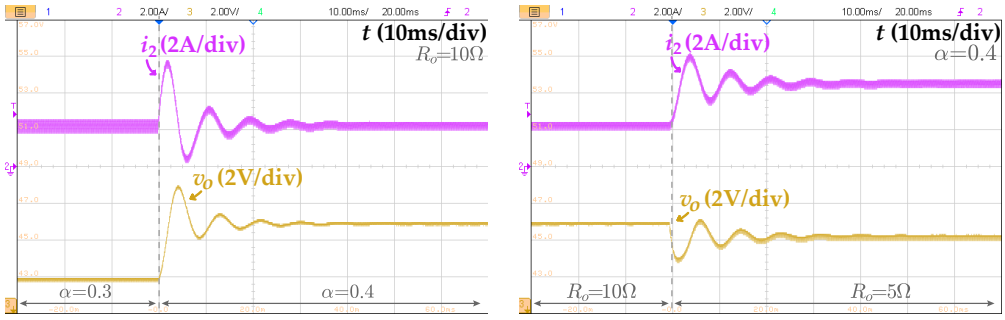


Figure 6. Experimental results and their expected results from simulation: Left hand-side: waveforms for $\alpha = 0.4$; Right hand-side: waveforms for $\alpha = 0.2$. (i) AC-link inductor current i_1; (ii) Output inductor current i_2; (iii) AC-link capacitor voltage v_1; (iv) AC-link capacitor voltage v_2; (v) Output capacitor voltage v_o.

3.2. Dynamics Results

In order to validate the dynamic behavior of the converter, step changes of α and resistive loads have been performed. Figure 7a depicts the response to a step change in α from 0.3 to 0.4, resulting in an increase of the output voltage and a decrease in L_2 inductor current due to α increment value. Additionally, a second-order oscillation is presented in the output voltage and output inductor current, as expected according to the model presented in (5) and (6). In Figure 7b, a similar oscillation is observed, but the output current increases while the output voltage is affected negatively due to the increase in the load current, decreasing sightly its value.



(**a**) (**b**)

Figure 7. Dynamic response of the converter: (**a**) Output inductor current i_2 and output capacitor voltage v_o for α step from 0.3 to 0.4 with $R_o = 10\ \Omega$; (**b**) Output inductor current i_2 and output capacitor voltage v_o for load step from $R_o = 10\ \Omega$ to 5 Ω with $\alpha = 0.4$.

As in the previous subsection, a detailed comparison between theoretical, simulation, and experimental dynamic results is presented in Figure 8. It is evident that the dynamics are quite similar, but the experimental dynamics are faster due to a small variation between the nominal and real passive component values. Moreover, it is noticeable that stabilization of the signal after the step change is faster in the experiment due to the presence of parasitic elements dampening the step response compared to the theoretical model from (5) and (6). Lastly, it is verified that the dynamic of the system is very close to the theoretical one, validating the hypothesis that the AC-link dynamics are much faster than the converter dynamics.

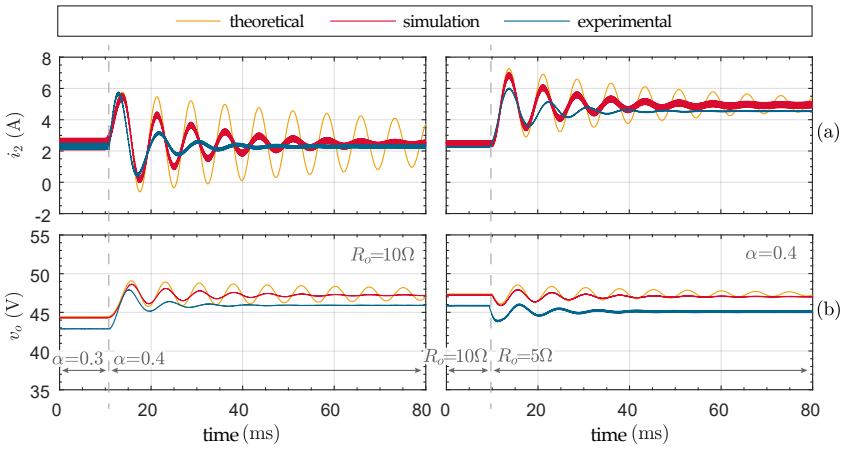


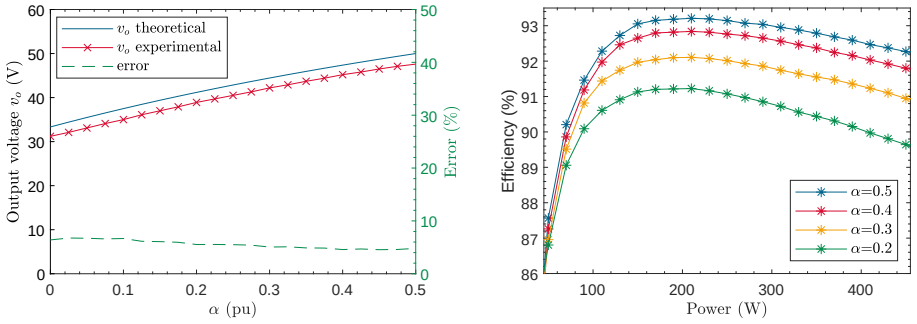
Figure 8. Experimental dynamics and their expected results from simulation and theoretical model: Left hand-side: α step from 0.3 to 0.4 with $R_o = 10\ \Omega$; Right hand-side: load step form $R_o = 10\ \Omega$ to 5 Ω with $\alpha = 0.4$. (**a**) Output inductor current i_2; (**b**) Output capacitor voltage v_o.

3.3. Voltage Gain and Efficiency

Finally, several measurements of the output voltage and input current were conducted to validate the converter voltage gain and to obtain an overview of the experimental efficiency of power conversion. Figure 9a displays the expected theoretical output voltage based on (8) in comparison to the experimental values. The figure illustrates the correlation between both signals and presents the error between them, which is lower than 7% and decreases as the output voltage increases. This demostrates the very good accuracy of the model, especially considering that the model only considers ideal components. The difference can be easily explained because of parasitic elements existing in the prototype. In terms of practical applications, for sizing purposes, the 7% error will not significantly affect the results, which are already subject to uncertainties due to component tolerances. On the other hand, the model is useful for the design of controllers during the implementation of

the converter in a given application. In this case, the error in the model will not affect the behavior of the system, since control methods often consider integral actuation, allowing to compensate modelling errors.

Additionally, to provide an estimation of the converter's performance, efficiency has been measured, as depicted in Figure 9b. It is possible to observe that the efficiency curves exhibit an operation region between 110 and 490 W where the prototype demonstrates the best performance. The converter shows an efficiency higher than 92% over a wide range of operations, with amaximum efficiency of 93.2% at 210 W for $\alpha = 0.5$. Moreover, it is noticeable that the performance increases for higher values of α, like classical PPC, since for higher α, output voltage is higher and, therefore, the converter reduction effort is lower. Efficiency of the converter is indeed related to voltage reduction gain and present similar results considering a fixed output and varying input voltages.



(**a**) (**b**)

Figure 9. Voltage gain error and efficiency of the proposed converter: (**a**) Theoretical and experimental output voltage correlation and experimental error; (**b**) Input and output power correlation and efficiency.

4. Discussion

4.1. Comparison with FB-PPC

As previously presented, the AC-link is proposed as an alternative to traditional PPCs, particularly concerning the FB-PPC presented earlier in Figure 2b. To carry out this comparison, the FB-PPC is constructed using the same components as the AC-link, with the difference being that instead of the impedance link used, a planar transformer with a turns ratio of 1:1 is employed. This allows a performance test under equal conditions for both converters from a load power range from 30 to 550 W, keeping the same values all other elements and interconnections, leading to comparative losses.

Efficiency of the FB-PPC for four values of voltage gains similar to the AC-link converter has been measured. When comparing these results with those obtained previously in Figure 9b, the efficiency curves in Figure 10 are obtained. It can be observed that in all voltage gain ranges, superior efficiency is achieved in the case of the AC-link, with a difference of up to 3.17% for a voltage gain of $G_v = 10/20$ in favor of the AC-link, and a difference of up to 7.21% for a voltage gain of $G_v = 7/17$ in favor of the AC-link. Since the test was conducted with the same components in both cases, the increase in losses is directly attributed to the transformer present in the PPC. Results from Figure 9b, validate clearly the interest of the proposed AC-link converter compared with traditional PPC, with important improvement in the efficiency over all operating range.

Additionally, in Figure 11, a simulation of dynamic behaviour of the proposed converter is compared with the classical PPC under same transient conditions introduced previously in Figure 8. It is interesting to mention that, although the waveforms do not match directly between the two due to their different central link composition, the behavior of the external dynamics between both converters is quite similar, as has been reported in the literature [22].

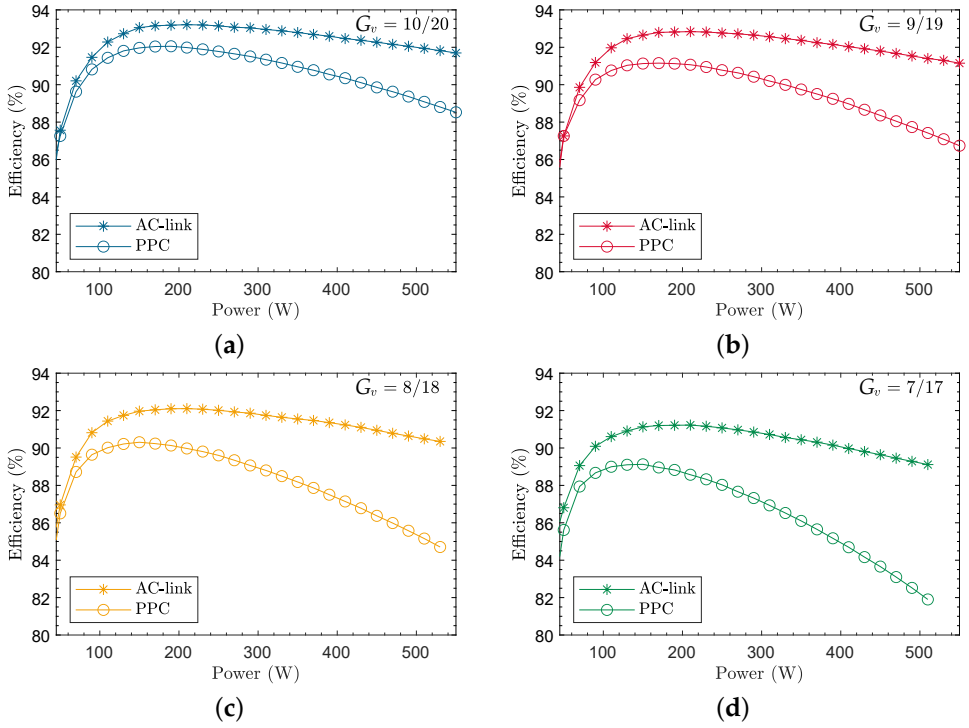


Figure 10. Efficiency comparison between proposed transformerless AC-link converter and FB-PPC step-down converters for different voltage gain: (**a**) $G_v = 10/20$; (**b**) $G_v = 9/19$; (**c**) $G_v = 8/18$; (**d**) $G_v = 7/17$.

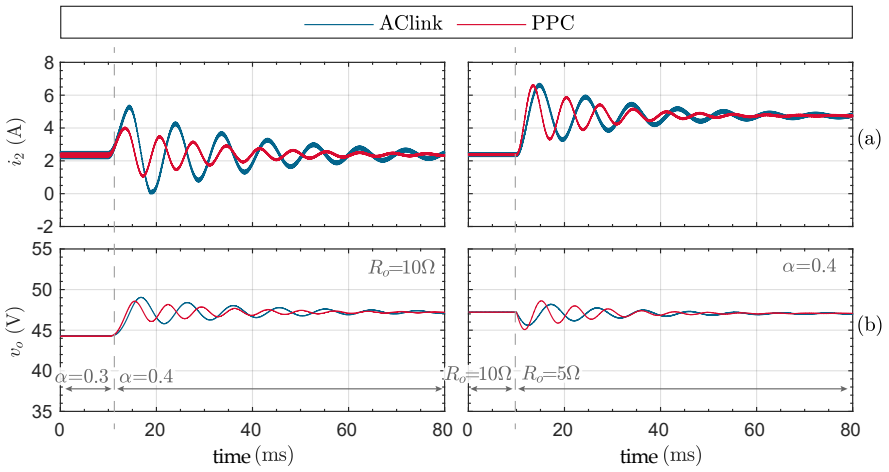


Figure 11. Dynamic simulation response of the proposed AC-link and conventional PPC converter: Left hand-side: α step from 0.3 to 0.4 with $R_o = 10\ \Omega$; Right hand-side: load step form $R_o = 10\ \Omega$ to 5 Ω with $\alpha = 0.4$. (**a**) Output inductor current i_2; (**b**) Output capacitor voltage v_o.

In terms of cost at a rated power of 300 W, it can be observed that the AC-link allows for significant cost savings by eliminating the use of the HFT compared to the PPC, which represents a great advantage in terms of manufacturing. In fact, in Table 3, we present a detailed comparison of the cost savings achieved by using the proposed converter compared to traditional PPC. Note that the total cost of the AC-link converter is \$184, while the cost of conventional PPC is \$346. Thus, the cost per Watt is reduced from 1.15 \$/W to 0.62 \$/W. Additionally, it is also possible to note that the AC-link converter slightly improves power density from 2.03 W/cm^3 to 2.78 W/cm^3.

Table 3. Detailed cost and volume comparison between AC-link and PPC construction.

Component	IGBT	HFT	Inductor	Capacitor	Gate-driver
Part number	IKZA75N120CH7XKSA1	PLA51LA32	1140-471K-RC	LGY2A821MELA25	-HANDCRAFTED-
Cost per unit, $	11.60	175.79	10.58	3.64	30
Vol. per unit, cm^3	1.54	81.62	29.49	12.27	-
AC-link					
Quantity	8	0	2	3	2
Cost, $	93	0	21	11	60
Volume, cm^3	12.31	0	58.97	36.82	-
PPC					
Quantity	8	1	1	2	2
Cost, $	93	176	11	7	60
Volume, cm^3	12.31	81.62	29.49	24.54	-

4.2. Comparison with Other Similar Solutions

In this section, brief comparisons with conventional PPC (also known as FB-PPC in the literature) and other similar DC–DC counterparts to derive the specific innovations of the proposed converter, have been expressed in terms of the number of different components, voltage stress, efficiency, power density, cost, and cost per Watt. The selected similar solutions operating at 300 W with the same number of power devices are: conventional dual-active-bridge (DAB) [23], non-isolated full bridge (NFB) in a buck operation [4], NFB in a boost operation [24], and step-down FB-PPC [13]. As shown in in Table 4, the specific innovations are summarized:

1. No HFTs are used in this proposed converter. Only inductors and capacitors are used as AC-links, highly reducing the overal cost of the implementation.
2. Peak efficiency is lower than its counterparts. In fact, the efficiency of any isolated converter is lower than that of a traditional sync-buck interleaving converter under the same power rating and power density [25]. Efficiency can be easily improved if e.g., IGBTs are replaced by FAST-IGBTs, MOSFETs-SiC or GaN devices.
3. The size is slightly smaller compared to its counterparts and the power density is improved because the HFT is not included. Further enhancements can be achieved by using smaller inductors and increasing parameters, such as the switching frequency (f_{sw}) from the current value of 10 kHz to 100 kHz.
4. Cost is lower with respect to topologies presented in [4,23,24] because HFT is avoided. This leads to a lower cost per Watt compared to other solutions, which is one of the main advantage of the proposed solution.

Table 4. Brief Comparison with other DC–DC counterparts at 300 W.

Solutions	**DAB [23]**	**NFB [4]**	**NFB (Boost) [24]**	**FB-PPC [13]**	**Here**
N^o of Semiconductors	8	8	8	8	8
N^o of Gate-Drivers	4	4	2	2	2
N^o of HFT	1	1	1	1	**0**
N^o of Inductors	1	2	3	1	2
N^o of Capacitors	1	1	4	2	3
Voltage Gain	αn	$\frac{\alpha}{2n+\alpha}$	$4\alpha(n+1)$	$\frac{2\alpha}{1+2\alpha}$	$\frac{1+2\alpha}{3+2\alpha}$
Voltage Stress	v_i	$v_i - v_o$	$v_i - v_o$	$v_i - v_o$	$v_i - v_o$
Full Load Eff., %	95.2	84.4	94.5	97.5	93.2
Size †, cm^3	135.7	165.2	231.5	148.0	108.1
Power Density, W/cm^3	2.21	1.82	1.30	2.03	2.78
Cost ‡ , $	403	413	375	346	184
Cost per Watt, $/W	1.34	1.38	1.25	1.15	0.62

† Gate driver size is neglected.; ‡ Costs derived from www.mouser.com, (accessed 08/17/2023), part numbers: IKZA75N120CH7XKSA1, PLA51LA32, 1140-471K-RC, LGY2A821MELA25 and an estimated driver cost around 30 per board.

5. Conclusions

In this paper, a transformerless partial power AC-link step-down DC–DC converter has been proposed and experimentally validated. Based on the PPC concept, the proposed converter has the advantage of not requiring an HFT that accounts for most of the manufacturing cost, which is replaced by an AC-link built with passive components only.

The operation of the proposed converter has been detailed, and a reduced-order dynamic average model has been derived. Experimental results based on a reduced-scale laboratory prototype have been provided to validate the interest of the proposed converter. Results were found to be consistent with theoretical expectations and simulations, both in terms of steady-state and dynamic behavior. The model of the converter is also validated, demonstrating high accuracy, since the error from comparing experimental and theoretical steady-state output voltages is lower than 7% across the entire operating range.

The efficiency of the proposed converter has also been measured. It is demonstarted that the proposed converter allows us to obtain an efficiency that is higher than 92% over a wide range of operational states, with a maximum efficiency of 93.2% at 210 W. Comparison with other state-of-the-art DC–DC converters of similar characteristics shows advantages of the proposed solutions, especially in terms of cost. Furthermore, experimental comparison with the PPC counterpart of the proposed solution has been conducted, demonstrating very interesting efficiency improvements in terms of efficiency over all the operation ranges, and up to 7% higher.

It is finally concluded that the proposed transformerless partial-power AC-link converter is very attractive for DC–DC step-down operation, and is a possible replacement for traditional PPC with possible applications in photovoltaic, battery charging, and DC microgrids, among others.

Author Contributions: Formal analysis, R.A.B. and H.R.; Investigation, R.A.B., H.R. and C.A.R.; Review and Editing, H.R. and A.M.L.; Funding acquisition, C.A.R and A.M.L. All authors have read and agreed to the published version of the manuscript.

Funding: This work was supported, in part, by the following projects from the Agencia Nacional de Investigacion y Desarrollo (ANID): ANID/FONDECYT Regular/1240537, AC3E (ANID/Basal/FB0008) and SERC Chile (ANID/FONDAP/1522A0006).

Data Availability Statement: No new data were created or analyzed in this study. Data sharing is not applicable to this article.

Conflicts of Interest: The authors declare no conflict of interest.

References

1. Rodriguez, J.; Blaabjerg, F.; Kazmierkowski, M.P. Energy Transition Technology: The Role of Power Electronics. *Proc. IEEE* **2023**, *111*, 329–334. [CrossRef]
2. dos Santos, N.G.; Zientarski, J.R.; da Silva, Martins, M.L. A Review of Series-Connected Partial Power Converters for DC–DC Applications. *IEEE J. Emerg. Sel. Top. Power Electron.* **2022**, *10*, 7825–7838. [CrossRef]
3. Rojas, C.A.; Kouro, S.; Perez, M.A.; Echeverria, J. DC–DC MMC for HVdc Grid Interface of Utility-Scale Photovoltaic Conversion Systems. *IEEE Trans. Ind. Electron.* **2018**, *65*, 352–362. [CrossRef]
4. Ye, S.; Eberle, W.; Liu, Y.F. A Novel Non-Isolated Full Bridge Topology for VRM Applications. *IEEE Trans. Power Electron.* **2008**, *23*, 427–437. [CrossRef]
5. Forouzesh, M.; Siwakoti, Y.P.; Gorji, S.A.; Blaabjerg, F.; Lehman, B. Step-Up DC–DC Converters: A Comprehensive Review of Voltage-Boosting Techniques, Topologies, and Applications. *IEEE Trans. Power Electron.* **2017**, *32*, 9143–9178. [CrossRef]
6. Liserre, M.; Perez, M.A.; Langwasser, M.; Rojas, C.A.; Zhou, Z. Unlocking the Hidden Capacity of the Electrical Grid Through Smart Transformer and Smart Transmission. *Proc. IEEE* **2023**, *111*, 421–437. [CrossRef]
7. Al-Baidhani, H.; Corti, F.; Reatti, A.; Kazimierczuk, M.K. Robust Sliding-Mode Control Design of DC–DC Zeta Converter Operating in Buck and Boost Modes. *Mathematics* **2023**, *11*, 3791. [CrossRef]
8. Zhu, Z.; Liu, X.; Kong, X.; Ma, L.; Lee, K.Y.; Xu, Y. PV/Hydrogen DC microgrid control using distributed economic model predictive control. *Renew. Energy* **2024**, *222*, 119871. [CrossRef]
9. Jarraya, I.; Abdelhedi, F.; Rizoug, N. An Innovative Power Management Strategy for Hybrid Battery–Supercapacitor Systems in Electric Vehicle. *Mathematics* **2024**, *12*, 50. [CrossRef]

10. Thounthong, P.; Mungporn, P.; Pierfederici, S.; Guilbert, D.; Bizon, N. Adaptive Control of Fuel Cell Converter Based on a New Hamiltonian Energy Function for Stabilizing the DC Bus in DC Microgrid Applications. *Mathematics* **2020**, *8*, 2035. [CrossRef]
11. Hossain, M.; Rahim, N. Recent progress and development on power DC–DC converter topology, control, design and applications: A review. *Renew. Sustain. Energy Rev.* **2018**, *81*, 205–230. [CrossRef]
12. Anzola, J.; Aizpuru, I.; Romero, A.A.; Loiti, A.A.; Lopez-Erauskin, R.; Artal-Sevil, J.S.; Bernal, C. Review of Architectures Based on Partial Power Processing for DC–DC Applications. *IEEE Access* **2020**, *8*, 103405–103418. [CrossRef]
13. Zapata, J.W.; Kouro, S.; Carrasco, G.; Renaudineau, H.; Meynard, T.A. Analysis of Partial Power DC–DC Converters for Two-Stage Photovoltaic Systems. *IEEE J. Emerg. Sel. Top. Power Electron.* **2019**, *7*, 591–603. [CrossRef]
14. Zientarski, J.R.; da Silva Martins, M.L.; Pinheiro, J.R.; Hey, H.L. Series-Connected Partial-Power Converters Applied to PV Systems: A Design Approach Based on Step-Up-Down Voltage Regulation Range. *IEEE Trans. Power Electron.* **2018**,*33*, 7622–7633. [CrossRef]
15. Daryaei, M.; Esteki, M.; Khajehoddin, S.A. High Efficiency and Full MPPT Range Partial Power Processing PV Module-Integrated Converter. *IEEE Trans. Power Electron.* **2023**, *38*, 6627–6641. [CrossRef]
16. Kim, N.; Parkhideh, B. PV-battery series inverter architecture: a solar inverter for seamless battery integration with partial-power DC–DC optimizer. *IEEE Trans. Energy Conv.* **2018**, *34*, 478–485. [CrossRef]
17. Mira, M.C.; Zhang, Z.; Jorgensen, K.L.; Andersen, M.A. Fractional Charging Converter With High Efficiency and Low Cost for Electrochemical Energy Storage Devices. *IEEE Trans. Ind. Appl.* **2019**, *55*, 7461–7470. [CrossRef]
18. Hoffmann, F.; Person, J.; Andresen, M.; Liserre, M.; Freijedo, F.D.; Wijekoon, T. A Multiport Partial Power Processing Converter With Energy Storage Integration for EV Stationary Charging. *IEEE J. Emerg. Sel. Top. Power Electron.* **2022**, *10*, 7950–7962. [CrossRef]
19. Renaudineau, H.; Rojas, C.; Kouro, S. Celda de Conmutación con Enlace de Potencia Interno. Patent App. PCT/CL2021/050112–WO2023087121A1, 2021.
20. Richard, E.; Renaudineau, H.; Llor, A.M.; Bugueño, R.A.; Rojas, C.A. Transformerless Partial Power AC-Link Converter for PV Integration to DC Microgrid. In Proceedings of the IECON 202248th Annual Conference of the IEEE Industrial Electronics Society, Brussels, Belgium, 17–20 October 2022.
21. Pesantez, D.; Renaudineau, H.; Rivera, S.; Kouro, S. Transformerless Partial Power Converter for Electric Vehicle Fast Charging Stations. In Proceedings of the 2022 IEEE Energy Conversion Congress and Exposition (ECCE), Detroit, MI, USA, 9–13 October 2022.
22. Wei, R.; Hou, N.; Ding, L.; Li, W.; Li, Y.R. A Fast Dynamic Response Control Method for the Hybrid SRC-PSFB Converter with Partial Power Processing Property. In Proceedings of the 2023 IEEE Energy Conversion Congress and Exposition (ECCE), Nashville, TN, USA, 29 October–2 November 2023; pp. 3279–3283.
23. Abramson, R.A.; Gunter, S.J.; Otten, D.M.; Afridi, K.K.; Perreault, D.J. Design and Evaluation of a Reconfigurable Stacked Active Bridge DC–DC Converter for Efficient Wide Load Range Operation. *IEEE Trans. Power Electron.* **2018**, *33*, 10428–10448. [CrossRef]
24. Radmanesh, H.; Dehbashi, A. An Integrated Non-Isolated Full-Bridge Converter with Soft Switching. In Proceedings of the 2019 International Power System Conference (PSC), Tehran, Iran, 9–11 December 2019; pp. 423–427.
25. Zheng, K.; Zhang, W.; Wu, X.; Jing, L.; Zhao, H. Partial Power Conversion for Increased Energy Storage Capability of Li-ion Battery Energy Storage System. *IEEE Trans. Ind. Electron.* **2023**, *71*, 4742–4752. [CrossRef]

Disclaimer/Publisher's Note: The statements, opinions and data contained in all publications are solely those of the individual author(s) and contributor(s) and not of MDPI and/or the editor(s). MDPI and/or the editor(s) disclaim responsibility for any injury to people or property resulting from any ideas, methods, instructions or products referred to in the content.